Journal of Power Sources 250 (2014) 110–119

Contents lists available at ScienceDirect

Journal of Power Sources

journal homepage: www.elsevier.com/locate/jpowsour

Three dimensional proton exchange membrane fuel cell cathode model using a modified agglomerate approach based on discrete catalyst particles

Firat C. Cetinbas, Suresh G. Advani*, Ajay K. Prasad

Center for Fuel Cell Research, Department of Mechanical Engineering, University of Delaware, Newark, DE 19716-3140, USA

HIGHLIGHTS

- New 3D model for PEMFC cathode developed with discrete catalyst particle approach.
- Good results obtained for reactant, reaction rate, and overpotential distributions.
- 3D model accurately predicts effect of Pt loading in the diffusion-loss region.

ARTICLE INFO

Article history:
Received 21 July 2013
Received in revised form
29 October 2013
Accepted 30 October 2013
Available online 9 November 2013

Keywords:
Catalyst layer model
Multiscale catalyst layer model
Spherical agglomerate model
Discrete particle approach
Pt particle model

ABSTRACT

The spherical agglomerate model represents the most detailed description of the PEM fuel cell catalyst layer as it accounts for both micro and macroscale transport phenomena. The usual approach with the classical spherical agglomerate model is to couple the homogenous mixture assumption for the agglomerate core to its idealized spherical geometry to obtain an analytical solution which is easily incorporated within a macroscale model. In this study, we incorporate numerical results from a modified agglomerate model based on discrete platinum particles [33] to create a more physically realistic 3D macroscale model for the PEM fuel cell cathode catalyst layer. Results from the 3D cathode model based on the modified particle approach are compared with the classical model and the macro-homogenous model. We find that, similar to the classical approach, the modified 3D model is able to reproduce previously reported trends for reactant, reaction rate, and overpotential distributions, whereas the macro-homogenous model fails to predict mass transport limitations properly. It is also shown that, unlike the classical approach, the modified 3D model is able to accurately predict the effect of Pt loading in the diffusion-loss region.

1. Introduction

Polymer electrolyte membrane (PEM) fuel cells are one of the most environmentally-friendly energy conversion devices, especially for the automotive industry. During the last decade, experimental and numerical approaches have been employed to investigate various aspects of PEM fuel cells. As a part of that ongoing research, computational models play an important role in the design and optimization of PEM fuel cells. The fidelity of computational models is highly dependent on an accurate description of the electrochemical phenomena occurring in the catalyst layer (CL) due to their critical impact on the performance and efficiency of the fuel cell.

It is a challenge to accurately model the CL because its structural and functional properties span the range from microscopic to macroscopic scales. The complex porous CL structure containing Pt, carbon support, ionomer electrolyte, gas pores, and liquid water clearly represents a multiscale, multiphase problem hosting a variety of reactions, and mass and heat transport phenomena. For device-level macroscale simulations, the literature presents some common approaches which can be broadly classified as interface models [1,2], homogeneous models [2–5], thin film models [6–9], and agglomerate models [10–33].

The simplest description of the CL is provided by the interface model in which a CL of infinitesimal thickness is considered between the membrane and the gas diffusion layer (GDL). The structure of the CL is ignored. The influence of catalytic activity is introduced by source terms that are used as the boundary condition at the membrane/GDL interface. This simplification neglects the

* Corresponding author.
E-mail address: advani@udel.edu (S.G. Advani).

0378-7753/$ – see front matter © 2013 Elsevier B.V. All rights reserved.
http://dx.doi.org/10.1016/j.jpowsour.2013.10.138

ohmic and diffusion resistances of the CL. Therefore, although the interface model is computationally efficient, it cannot predict the cell performance correctly. The 3D PEM fuel cell model of Berning et al. [1] represents a good example of the interface model. Harvey et al. [2] reported that current densities are overestimated by the interface model.

The macro-homogeneous model represents the CL as a porous matrix consisting of a uniform mixture of Pt, carbon, and electrolyte. Gas phase reactants diffuse through the porous matrix to the reaction sites. Ions and electrons are assumed to travel through the electrolyte and the carbon network, respectively. Therefore, diffusive and ohmic transport resistances are taken into account based on effective medium theory. However, the macro-homogeneous model cannot predict mass transport correctly, and is therefore unable to provide a limiting current density. This shortcoming can be clearly observed in the results of Rho et al. [3], Wang et al. [4], and Eikerling et al. [5].

The thin film model is almost identical to the macro-homogeneous model and employs the same type of CL structure. However, in contrast to the macro-homogeneous model, the gas pores are assumed to be flooded with liquid water. Therefore, reactant gases must first dissolve in liquid water in order to be transported to the reaction sites. This model results in high diffusive resistances so a thin CL (i.e. thin film) must be assumed to obtain a match with the experimental results. Unlike the homogeneous model, the thin film model is able to predict the limiting current density [6–9].

Among the device-level modeling approaches, the most detailed representation of the CL is provided by the agglomerate models. Unlike the previously mentioned methods, only the agglomerate approach considers the CL as a multi-scale problem. The porous structure of the CL is assumed to consist of gas pores and agglomerates (with an assumed microstructure) that are covered by an electrolyte film. The agglomerate itself is assumed to consist of a homogeneous mixture of carbon-supported catalyst and electrolyte as depicted in Fig. 1. In this model, reactant gases travel through the gas pores until they reach the electrolyte film that covers the agglomerates. The gases then dissolve into the electrolyte film and are transported by diffusion inside the agglomerate to the reaction sites.

In recent years, there have been many developments in CL modeling. Inexpensive computational power has made it feasible to model the actual CL microstructure [34–43]. In addition, some researchers have proposed modifications to the classical agglomerate model. For example, Jain et al. [30] compared spherical, cylindrical, and planar agglomerate geometries and showed that the nature of the microscale geometry affects O_2 consumption. Epting and Litster [31] examined the importance of agglomerate size distribution based on nano-CT imaging of a typical CL, and concluded that the size distribution has a significant impact on the results. Kamarajugadda and Mazumder [32] considered two overlapped agglomerates with unequal radii as a generalized shape for agglomeration. They incorporated numerical simulations of their 3D agglomerate as a sub-grid-scale model into their 2D PEM fuel cell model, and found that while the agglomerate shape is unimportant for small agglomerates, it becomes significant for larger agglomerates.

One of the main assumptions of the classical agglomerate model is that the agglomerate core consists of homogenous mixture of C|Pt particles and the ionomer. A consequence of this assumption is that the model's results become insensitive to Pt loading at high current densities. Cetinbas et al. [33] proposed a modified microstructure for the agglomerate core by introducing discrete Pt particles. They concluded that the presence of discrete catalyst particles leads to a proper accounting of the diffusion process inside the agglomerate core. Therefore, unlike the classical approach, the modified model was shown to accurately predict the effect of catalyst loading in the diffusion-loss region.

In this study, the microscale approach proposed in Ref. [33] is incorporated into a 3D single channel PEM fuel cell cathode model. However, unlike the classical agglomerate approach, the modified approach does not lend itself to an analytical solution which is easily coupled to the macroscale model. Therefore, the coupling method used in Ref. [19] has to be modified in order to interface with the numerical results from the discrete particle approach. Accordingly, the numerical solution obtained from the 2D microscale model is expressed as a function of macroscale model variables and then incorporated within the 3D cathode model. In addition, we compare the predictions of the macro-homogenous, classical, and modified agglomerate approaches by plotting their polarization curves and current density distributions. Finally, we investigate the sensitivity of the different agglomerate models to Pt loading.

2. Cathode model

We have implemented a 3D, single channel, isothermal, steady-state cathode model that accounts for the conservation of mass, momentum, chemical species, electrons, and ions. The CL is modeled by the macro-homogenous, classical, and modified agglomerate approaches which will be explained in the subsequent sections. Symmetry in the single channel is exploited to reduce the computational domain such that it encompasses half of the channel

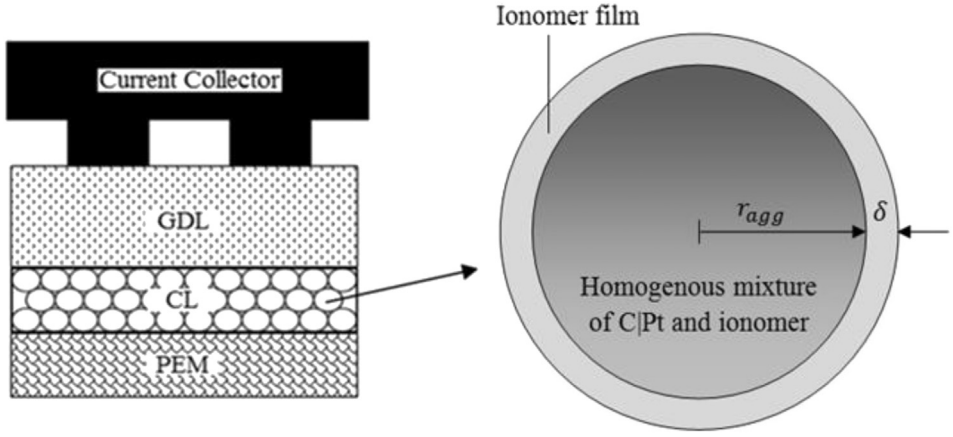

Fig. 1. Schematic of the catalyst layer structure in the classical spherical agglomerate approach.

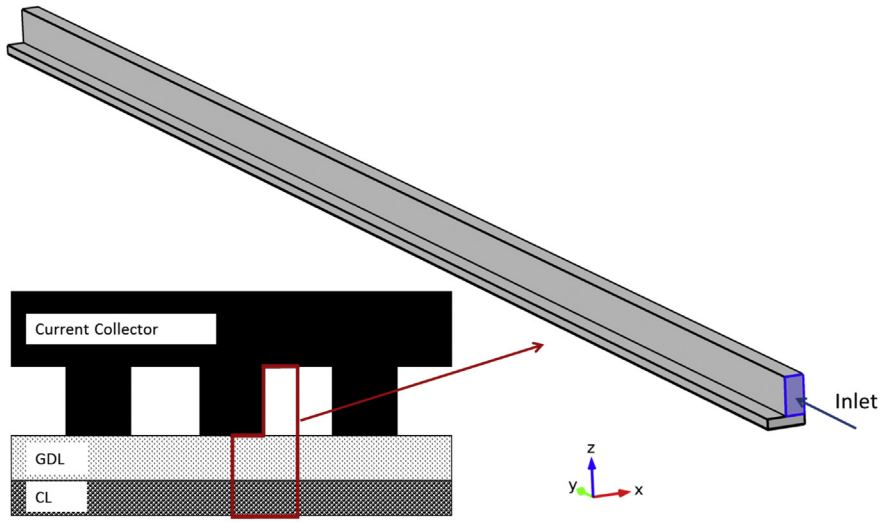

Fig. 2. Computational domain for the 3D cathode model.

and half of the land area as illustrated in Fig. 2. The domain dimensions are listed in Table 1. The highly-coupled equations that govern the electrochemical and transport phenomena within the cell are solved with the finite element software COMSOL 4.2.

Assuming laminar, incompressible flow, mass and momentum conservation in the gas channel are governed by the following equations:

$$\nabla\cdot\boldsymbol{u} = 0 \tag{1}$$

$$\rho(\boldsymbol{u}\cdot\nabla)\boldsymbol{u} = -\nabla p + \nabla\cdot\mu\left(\nabla\boldsymbol{u} + (\nabla\boldsymbol{u})^{\boldsymbol{T}}\right) \tag{2}$$

where $\boldsymbol{u}$ is the velocity field, p is pressure, ρ is density and μ is dynamic viscosity. In the porous domains (GDL and CL) the flow is described by the Brinkman equation which extends Darcy's law to account for the momentum balance.

$$\rho\nabla\cdot\boldsymbol{u} = Q \tag{3}$$

$$\frac{\rho}{\varepsilon}\left((\boldsymbol{u}\cdot\nabla)\frac{\boldsymbol{u}}{\varepsilon}\right) = -\nabla p + \nabla\cdot\frac{\mu}{\varepsilon}\left(\nabla\boldsymbol{u} + (\nabla\boldsymbol{u})^{\boldsymbol{T}}\right) - \nabla\cdot\frac{2\mu}{3\varepsilon}(\nabla\cdot\boldsymbol{u}) - \left(\frac{\mu}{k} + Q\right)\boldsymbol{u} \tag{4}$$

where Q is the mass source term which is calculated from the reactions in the CL, ε is the porosity, and k is the permeability of the GDL.

The diffusion of oxygen, water vapor, and nitrogen in the cathode is described by using the Maxwell–Stefan equations including the effect of convection.

$$\nabla\cdot\left[-\rho\omega_j\sum_k D_{jk}^{\text{eff}}\nabla\frac{\omega_k}{M_k}M_{\text{n}}\right] + \rho(\boldsymbol{u}\cdot\nabla)\omega_j = R_j \tag{5}$$

Eq. (5) solves for the mass fraction (ω_j) of each chemical species with R_j representing the source term due to electrochemical reactions in the CL. The diffusion coefficients for different operating conditions can be calculated based on the reference values of binary diffusivities [44]:

$$D_{ij} = D_{ij}^{\text{ref}}\left(\frac{p_{\text{ref}}}{p}\right)\left(\frac{T}{T_{\text{ref}}}\right)^{1.75} \tag{6}$$

where the reference pressure (p_{ref}) is 1 atm, the reference temperature (T_{ref}) is 298 K, and the reference diffusivities D_{ij}^{ref} used are listed in Table 2.

The density of the mixture, which is also used in the mass and momentum conservation equations, is calculated using the ideal gas law as follows.

$$\rho = \frac{M_{\text{n}}P}{RT} \quad \text{where } M_{\text{n}} = \left(\sum_j\frac{\omega_j}{M_j}\right)^{-1} \tag{7}$$

The Bruggeman approximation is commonly used to calculate the effective properties of isotropic porous structures. Here, we use this approximation to calculate the effective diffusivities.

$$D_{jk}^{\text{eff}} = D_{jk}\varepsilon_i^{1.5} \tag{8}$$

where ε_i represents the porosity of the corresponding domain. Charge transport by the electron and ion phases is governed by the following equations.

$$\nabla\cdot\left(\sigma_{\text{m}}^{\text{eff}}\nabla\varnothing_{\text{m}}\right) = \nabla\cdot i \tag{9}$$

$$\nabla\cdot\left(\sigma_{\text{s}}^{\text{eff}}\nabla\varnothing_{\text{s}}\right) = -\nabla\cdot i \tag{10}$$

Table 1
Geometric parameters for the single channel computational domain.

Channel length	L_{ch}	50 [mm]
Channel height	h_{ch}	1 [mm]
Channel width	w_{ch}	1 [mm]
Land width	w_{l}	1 [mm]
GDL thickness	t_{GDL}	250 [μm]
CL thickness	t_{CL}	15 [μm]

Table 2
Binary diffusivities at 1 atm and 298 K [44].

$D_{O_2N_2}^{\text{ref}}$	2.07×10^{-5} [$m^2\ s^{-1}$]
$D_{O_2H_2O}^{\text{ref}}$	2.64×10^{-5} [$m^2\ s^{-1}$]
$D_{N_2H_2O}^{\text{ref}}$	2.64×10^{-5} [$m^2\ s^{-1}$]

where σ_m^{eff} and σ_s^{eff} are the effective ion and electron conductivities, $\varnothing_m$ and $\varnothing_s$ are ionic and electronic potentials, and $\nabla.i$ is the volumetric current density. The Bruggeman approximation is again used to calculate the effective conductivities.

$$\sigma_j^{eff} = \sigma_j \varepsilon_i^{1.5} \tag{11}$$

The ionic conductivity (σ_m) is dependent on the local water content and temperature. In order to determine the local ionic conductivity we used the empirical relation reported by Springer et al. [45] for Nafion™.

$$\sigma_m = 100\left(5.139\times10^{-3}\lambda - 3.26\times10^{-3}\right)\exp\left[1268\left(\frac{1}{303}-\frac{1}{T}\right)\right] \tag{12}$$

where λ is the local water content which is expressed as a function of local relative humidity as [19]:

$$\lambda = 0.3 + 10.8\phi_{RH} - 16\phi_{RH}^2 + 14.1\phi_{RH}^3 \tag{13}$$

where ϕ_{RH} is the local relative humidity.

The effects of the electrochemical reaction on charge and reactant transport are described by the source terms in the governing equations. The O_2 and H_2O source terms in the CL domain (R_{O_2} and R_{H_2O}) are calculated from Faraday's law:

$$R_{O_2} = -\frac{\nabla\cdot i}{4F} \tag{14}$$

$$R_{H_2O} = \frac{(\alpha_{OD}+1)\nabla\cdot i}{2F} \tag{15}$$

where α_{OD} is the osmotic drag coefficient which can be written as a function of the nominal cathode overpotential (η_{NCO}) as [19]:

$$\alpha_{OD} = \begin{cases} 1.0 & \eta_{NCO} < 0.25 \\ 46\eta_{NCO}^2 - 31.52\eta_{NCO} + 5.7 & 0.25 \le \eta_{NCO} \le 0.35 \\ 0.3 & \eta_{NCO} > 0.35 \end{cases} \tag{16}$$

The nominal cathode overpotential (η_{NCO}) can be defined as the measure of total losses (including activation and ohmic losses) in the cathode. It can be expressed as [19]:

$$\eta_{NCO} = \varnothing_s|_{\text{Current Collector}} - \varnothing_m|_{\text{Membrane–CL Interface}} \tag{17}$$

where the electron potential at the current collector and ion potential at the membrane–CL interface are the boundary conditions for the charge conservation equations. All the boundary conditions are clarified later. For the sake of simplicity our model considers only the cathode electrode as the majority of the activation loss occurs in the cathode, whereas the reactions at anode are several orders of magnitude faster. Neglecting the losses in anode and membrane, the cathode potential can be expressed as [19]:

$$V_c = E_{th} - \eta_{NCO} \tag{18}$$

$$E_{th} = 1.229 - 8.456\times10^{-4}(T-295.15) + 4.31\times10^{-5}T\left[\ln(P_{H_2}) - \frac{1}{2}\ln(P_{O_2})\right] \tag{19}$$

2.1. Spherical agglomerate model

Catalyst layer modeling techniques are required to obtain an expression for the volumetric current density ($\nabla.i$) which quantifies the rate of the electrochemical reaction occurring within the CL. As stated earlier, the spherical agglomerate approach is the most comprehensive description of the CL as it accounts for reaction-diffusion phenomena inside the imaginary microstructures called agglomerates. It is a multi-scale approach that ranges from the agglomerate at the microscale to the entire CL at the macroscale.

The mass balance of O_2 in the CL can be written in terms of the agglomerate flux or total reaction rate in the CL as [19]:

$$\nabla\cdot N_{O_2} + a_{agg}N_{O_2}^{agg} = 0 \tag{20}$$

$$\nabla\cdot N_{O_2} + R_{O_2}^{total} = 0 \tag{21}$$

where a_{agg} is the ratio of total agglomerate surface area to CL volume, $N_{O_2}^{agg}$ is the O_2 flux at the surface of a single agglomerate, and $R_{O_2}^{total}$ is the total reaction rate in CL. Sun et al. [19] tied the microscale agglomerate to the macroscale CL by noting the equality between Eqs. (20) and (21) and obtained an expression for $\nabla.i$. Kamarajugadda and Mazumder [32] used only Eq. (21) to integrate their 3D numerical agglomerate into a 2D device-scale simulation. In this study, we use Eq. (20) to derive the volumetric current density. The goal is to develop a procedure to couple the 2D numerical results of the modified agglomerate problem in Ref. [33] with a 3D cathode model.

The classical agglomerate problem can be summarized as a reaction-diffusion process in the homogenous agglomerate core following the pure diffusion of reactant through the ionomer film. For simplicity, the problem is solved in a 1D spherically-symmetric domain as in Fig. 3. The goal is to calculate the reaction rate per unit volume by obtaining the analytical solution of Eqs. (22) and (23).

$$\frac{D_{eff}}{r^2}\frac{d}{dr}\left(r^2\frac{dC}{dr}\right) = k_c C \quad \text{in agglomerate core} \tag{22}$$

$$\frac{D}{r^2}\frac{d}{dr}\left(r^2\frac{dC_f}{dr}\right) = 0 \quad \text{in ionomer film} \tag{23}$$

where D is the diffusivity of O_2 in the ionomer film which is curve-fitted in Ref. [19] using the experimental data of Ref. [47] as:

$$D = 0.0438\exp\left(\frac{-25\ \text{kJ mol}^{-1}}{RT}\right)\ \text{cm}^2\ \text{s}^{-1} \tag{24}$$

D_{eff} is the effective diffusivity of O_2 in the agglomerate core which is calculated from the Bruggeman correlation, and k_c is the is the reaction rate constant given by the Butler–Volmer type expression as:

$$k_c = \frac{a_{Pt}}{4F}\frac{i_0^{ref}}{C_{O_2,ref}}\left[\exp\left(-\frac{\alpha_c F}{RT}\varphi\right) - \exp\left(\frac{(1-\alpha_c)F}{RT}\varphi\right)\right] \tag{25}$$

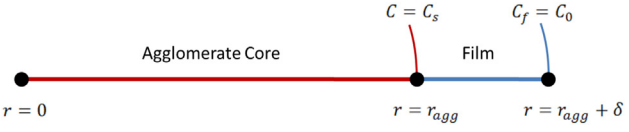

Fig. 3. 1D spherical agglomerate domain and boundary conditions.

where a_{Pt} is the total reaction area per unit volume of agglomerate, i_0^{ref} is the reference exchange current density, $C_{O_2,ref}$ is the standard reference O_2 concentration, α_c is the charge transfer coefficient, and φ is the local over-potential in the CL domain. The total reaction area per unit volume of the agglomerate is expressed as:

$$a_{Pt} = A_0 \frac{m_{Pt}}{t_{CL}(1-\varepsilon_{CL})} \tag{26}$$

where A_0 is the catalyst surface area per unit mass, m_{Pt} is the catalyst loading (kg m^{-2}), and t_{CL} is the thickness of the catalyst layer.

Parthasarathy et al. [46–48] reported two Tafel slopes corresponding to high and low current regimes. In order to account for the variation in Tafel slope, we used two distinct values for the exchange current density (i_0^{ref}), and the charge transfer coefficient (α_c) as given in Table 3.

It is important to note that the overpotential within the agglomerate (φ_{agg}) is assumed to be constant due to the agglomerate's small size. On the other hand, the macroscale overpotential (φ) is a variable governed by the charge transport equations. Selecting the oxygen electrode as the reference electrode with zero potential, the local overpotential in the CL domain can be expressed simply as the difference between the electronic and ionic potentials.

$$\varphi = \varnothing_s - \varnothing_m \tag{27}$$

Using the solution procedure outlined in Ref. [49] the O_2 concentration within the agglomerate core and the ionomer film (solutions for Eqs. (22) and (23)) are given by:

$$C(r) = C_s \frac{\sinh\left(\mathrm{Th}\frac{r}{r_{agg}}\right)}{\frac{r}{r_{agg}}\sinh(\mathrm{Th})} \quad \text{in the agglomerate core} \tag{28}$$

$$C_f(r) = \frac{\left(-D_{eff}\frac{dC}{dr}\right)r_{agg}^2}{D}\left(\frac{1}{r}-\frac{1}{r_{agg}+\delta}\right) + C_0 \quad \text{in the ionomer film} \tag{29}$$

Table 3
Parameters used in PEM fuel cell cathode model simulations.

Pressure P	15,1987.5 Pa
Temperature T	353 K
Relative humidity RH	0.5
Stoichiometry λ_{ST}	2
O_2 mass fraction y_{O_2}	0.209
H_2O mass fraction y_{H_2O}	0.102
GDL porosity ε_{GDL}	0.4
CL porosity ε_{CL}	0.1
Ionomer vol. fraction in agglomerate ε_{agg}	0.5
GDL permeability k_{GDL}	1.45e−11 m^2
CL permeability k_{CL}	1.45e−11 m^2
Platinum loading m_{Pt}	4e−3 kg m^{-2}
Platinum particle radius r_{Pt}	5e−9 m
Agglomerate radius r_{agg}	1e−6 m
Effective agglomerate area a_{agg}	3.6e5 m^{-2} m^{-3}
Ionomer film thickness δ	80e−9 m
Reference O_2 concentration $C_{O_2,ref}$	0.85 mol m^{-3}
Henry's constant H	31,663 Pa m^3 mol^{-1}
Reference exchange current density $i_{0,ref}$	3.86e−4 A m^{-2} for $V_c \geq 0.8$ V 1.46e−2 A m^{-2} for $V_c \leq 0.8$ V
Cathodic transfer coefficient α_c	1 for $V_c \geq 0.8$ V 0.617 for $V_c \leq 0.8$ V
Electron conductivity σ_s	100 S m^{-1}

where Th is the dimensionless Thiele modulus defined as the ratio of the surface reaction rate and the diffusion rate through the catalyst pellet:

$$\mathrm{Th} = r_{agg}\sqrt{\frac{k_c}{D_{eff}}} \tag{30}$$

Referring back to Eq. (20) and Fig. 3, the reactant flux on the agglomerate core surface can be written in terms of reactant concentrations using Fick's law for the 1D spherically-symmetric domain as:

$$N_{O_2}^{agg} = D\frac{r_{agg}+\delta}{r_{agg}}\left(\frac{C_0 - C_s}{\delta}\right) \tag{31}$$

where C_s can be expressed in terms of C_0 using Eqs. (28) and (29) as:

$$C_s = \frac{C_0}{1+\frac{D_{eff}}{D}\left(\frac{\delta}{r_{agg}+\delta}\right)(\mathrm{Th}\coth(\mathrm{Th})-1)} \tag{32}$$

Similar to the overpotential, C_0 is assumed constant for a given agglomerate, whereas it varies across agglomerates within the macroscale CL domain. Within the macroscale domain, C_0 can be found by Henry's law as:

$$C_0 = \frac{P_{O_2}}{H} \tag{33}$$

where P_{O_2} is the partial pressure of O_2, and H is Henry's constant. Finally, using Faraday's law and Eq. (20), the volumetric current density is obtained as follows:

$$\nabla\cdot i = -4F\nabla\cdot N_{O_2} = 4Fa_{agg}N_{O_2}^{agg} \tag{34}$$

$$\nabla\cdot i = 4Fa_{agg}\frac{P_{O_2}}{H}\left(\frac{\frac{D_{eff}}{r_{agg}}(\mathrm{Th}\coth(\mathrm{Th})-1)}{1+\frac{D_{eff}}{D}\left(\frac{\delta}{r_{agg}+\delta}\right)(\mathrm{Th}\coth(\mathrm{Th})-1)}\right) \tag{35}$$

Equation (35) includes two macroscale variables, P_{O_2} and φ (embedded in the Th term), which are related to the microscale parameters C_0 and φ_{agg}. All the remaining parameters are constants relating to the material and geometric properties of the microstructure. So Eq. (35) gives the current generation per unit volume of the CL in terms of reactant concentration and overpotential by representing the effect of CL microscale agglomerate structure (without solving the microscale problem).

2.2. Modified agglomerate model

The modified agglomerate model presented in Ref. [33] employs random distributions of Pt particles inside the agglomerate core instead of the homogenous mixture assumption in the classical approach. In the modified approach, the reaction-diffusion problem needs to be solved numerically, whereas the classical model has an analytical solution. Therefore, the micro to macroscale coupling procedure here is based on a numerical solution. In addition, unlike the classical spherical 1D approach, the modified approach employed a 2D cylindrical agglomerate configuration for computational efficiency with very little loss in accuracy. One can refer to [33] for further details about the modified approach.

Equation (35) can now be applied to accept numerical results from the modified microscale model. The goal is to couple the modified model in a way that eliminates the need to numerically solve for the microscale model at every grid point. Equation (34) indicates that we need to solve for $N_{O_2}^{agg}$ at the microscale in order

to obtain the local value of the current generation per unit volume of the CL. Furthermore, Eq. (35) indicates that $N_{O_2}^{agg}$ can be expressed as a function of microscale parameters C_0 and φ_{agg}, which can be written in terms of macroscale parameters P_{O_2} and φ. So we simulated the modified microscale model for various values of C_0 and found that $N_{O_2}^{agg}$ varies linearly with C_0, and also with the macroscale parameter P_{O_2}. We conducted the simulations for agglomerate overpotentials φ_{agg} between 0 and 1 V and obtained a curve (called the agglomerate characteristic curve) for $N_{O_2}^{agg}$ vs. φ_{agg}. Next, we fitted a polynomial to this characteristic curve and expressed it in terms of C_0. Finally, the volumetric current density of the CL was obtained as:

$$\nabla \cdot i = 4Fa_{agg}\frac{P_{O_2}}{HC_{0,ref}^{agg}} f(\varphi) \tag{36}$$

where $C_{0,ref}^{agg} = 8$ mol m^{-3} is the reference C_0 value, and $f(\varphi)$ is the polynomial fit to the $N_{O_2}^{agg}$ vs. ϕ_{agg} characteristic curve.

It is important to note that the characteristic curves for the modified agglomerate model vary in the diffusion-limited region, as shown in Fig. 5, depending on the specific distribution of catalyst particles in the agglomerate core. This is because variations in the randomly-generated distributions result in differences in diffusion at the particle level, leading to different limiting currents as explained in Ref. [33]. Reference [33] provides details on the effect of particle locations on diffusion losses. Hence it is necessary to average the results across an adequate number of samples with random distributions. We investigated samples containing 10, 20 and 30 random distributions of catalyst particles and obtained standard deviations of their limiting current densities as 0.048, 0.044, and 0.0441 A cm^{-2}, respectively. It was decided that a sample size of 20 was adequate to obtain a reliable average of the diffusion-loss behavior of agglomerates as shown in Fig. 5.

We assessed the accuracy of the modified agglomerate model as shown in Fig. 6. First, we validated our COMSOL code by comparing our numerically obtained polarization curve for the 1D spherically-symmetric agglomerate model with its analytical solution. As Fig. 6 indicates, the comparison is perfect. Next, we

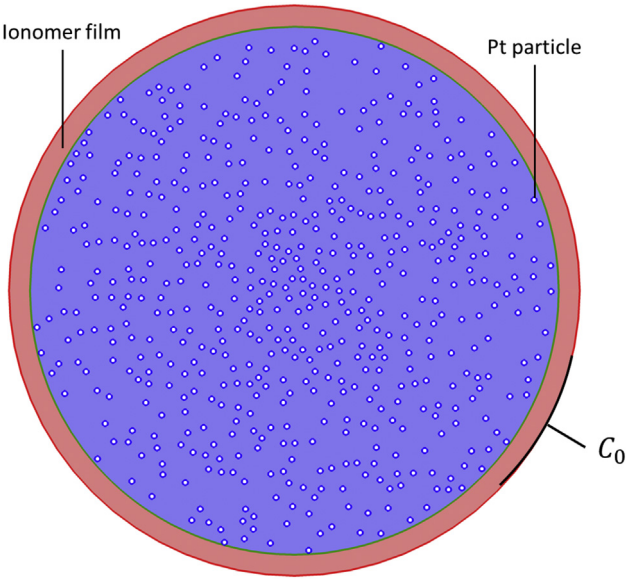

Fig. 4. 2D cylindrical computational domain for the modified agglomerate model in which Pt particles can be randomly or selectively distributed.

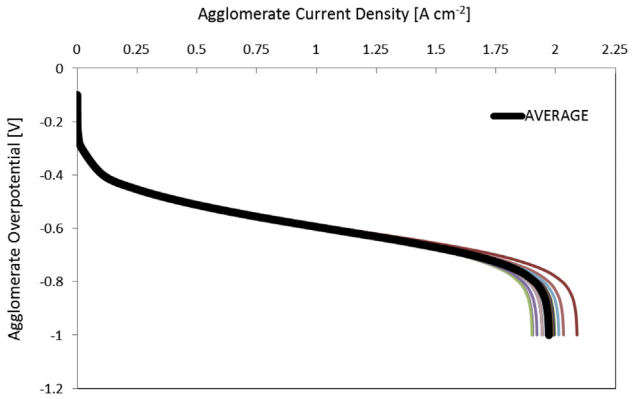

Fig. 5. Agglomerate polarization curves from the modified approach for 20 different random particle distributions ($m_{Pt} = 0.4$ mg cm^{-2}).

investigated the loss in accuracy incurred by using a 2D cylindrical agglomerate approximation in place of a spherically symmetric one. As previously mentioned, the 2D formulation is preferred as it is computationally more efficient [33]. Fig. 6 shows that the polarization curve from the 2D simulation differs from the analytical solution in the diffusion loss region, but the difference is acceptably small. Next, we plot the polarization curve obtained with the discrete particle model. It is immediately apparent that our modified particle approach predicts much higher diffusion losses compared to the classical approach. As explained in Ref. [33], this is because the outermost particles in a random distribution may be situated some distance away from the ionomer film (see Fig. 4) leading to a higher effective film thickness, and hence higher diffusion losses. Accordingly, when we reduced the thickness of the ionomer film in the discrete particle model, we found that it was possible to match the limiting current predicted by the classical model. Such a tuning process is employed by many other modeling studies which adjust agglomerate structural parameters to match experimental results.

2.3. Macro-homogenous model

In order to show the importance of multiscale modeling, we will also compare the agglomerate model results with the macro-homogenous model. The macro-homogenous model does not consider a microscale structure for the CL; instead, the CL is represented using an effective medium theory for which it is only necessary to calculate the effective diffusion properties for charge and species transport. The volumetric current density is then

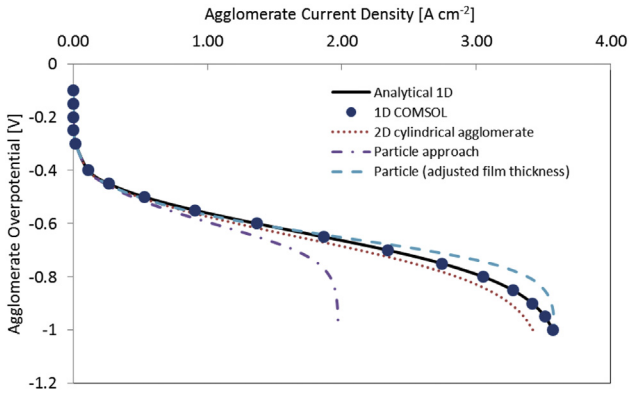

Fig. 6. Agglomerate polarization curves for various microscale models.

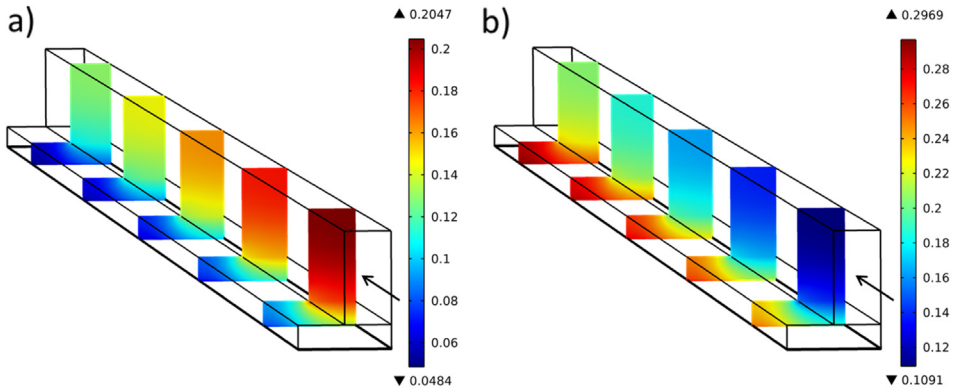

Fig. 7. Mass fraction distribution in the cathode at $V_c = 0.2$ V (a) O_2, and (b) H_2O. The cross-section includes the channel, the GDL, and the catalyst layer.

calculated from the Butler–Volmer equation. The area term a_{scale} is used as a fitting parameter as in Ref. [2] to match results with the agglomerate models.

$$\nabla \cdot i = a_{scale} i_0^{ref} \frac{C_{O_2}}{C_{O_2,ref}} \left[\exp\left(-\frac{\alpha_c F}{RT} \varphi \right) - \exp\left(\frac{(1-\alpha_c)F}{RT} \varphi \right) \right] \quad (37)$$

2.4. Boundary conditions and model parameters

The model parameters and operating conditions for our simulations are provided in Table 3. For the conservation of mass and momentum, a laminar inflow boundary condition was used with a specified inlet velocity, and an outlet pressure was specified as the outflow boundary condition. The air inlet velocity is calculated from the operating conditions listed in Table 3. The mass fractions at the air inlet are also calculated from the given operating conditions and used to specify the inlet boundary conditions for the Maxwell–Stefan equations. For the diffusion of electrons, we set $\varphi = 0$ along the surface of the current collector rib, and zero flux at the membrane/CL interface. For ionic charge transport, the ion potential at the current collector is set to zero, whereas the ion potential at the membrane/CL interface is set to η_{NCO}. Symmetry boundary conditions are applied as appropriate in the transverse (x–z) plane (see Fig. 2) for each governing equation.

3. Results and discussion

The modified microscale agglomerate model in Ref. [33] was coupled to the macroscopic 3D cathode model using COMSOL. First, we focus on the general trends obtained with the 3D single channel cathode model using the modified agglomerate approach (with adjusted film thickness). The goal is to confirm that the coupling works properly. Subsequently, we will compare our 3D cathode model results coupled using the modified agglomerate model approach with the 3D cathode model coupled to the classical agglomerate model and the macro-homogenous model.

Mass fraction contours of O_2 and H_2O (vapor) are presented for the diffusion-loss regime in Fig. 7a and b, respectively. As expected, O_2 is being depleted as it passes through the channel. In addition, the O_2 concentration is always higher under the channel than under the land, which implies a higher reaction rate under the channel. Again as expected, the product water vapor concentration increases towards the outlet of the channel.

Fig. 8 shows the overpotential distribution through the CL thickness under three different operating regimes. Consistent with the results in Ref. [19], the overpotential distributions in Fig. 8 are seen to be nonuniform. As in Ref. [19], the overpotential is always higher under the land because of shorter electron paths that reduce ohmic losses. The difference in overpotential between the land and channel regions increases with reaction rate because the ohmic losses become more noticeable at higher current densities. It is also important to note that reaction rate, and so the current density distribution, is an exponential function of overpotential. Therefore, even the small variations shown in Fig. 8 can significantly affect the current density distribution.

Volumetric current density is plotted along the longitudinal (x–y) plane occupied by the membrane/CL interface in Fig. 9 for three different operating regimes. At low current densities (NCO = 0.3 V), the reaction rate is slow enough that O_2 diffusion is not the limiting factor. Therefore, the reaction rate is maximized under the land due to reduced ohmic losses as shown in Fig. 8. On the other hand, at high current densities (NCO = 1.0 V), mass transport losses begin to

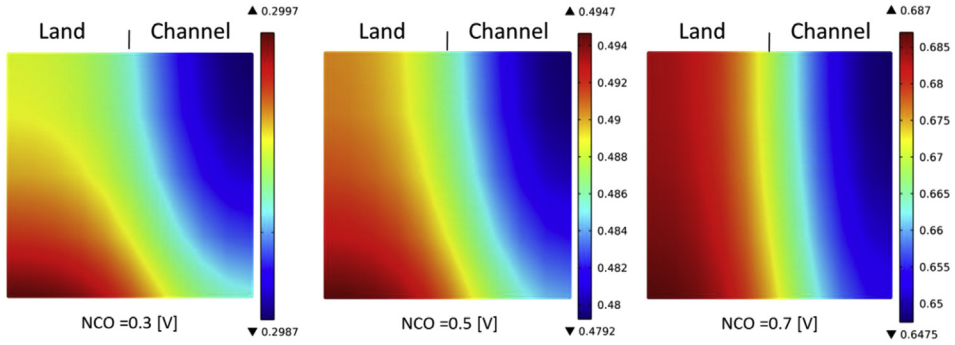

Fig. 8. Cathode overpotential (φ) distribution across the CL thickness from the modified agglomerate approach along the transverse (x–z) plane at $y = 0.95L_{ch}$. The bottom boundary of the plot corresponds to the CL/membrane interface.

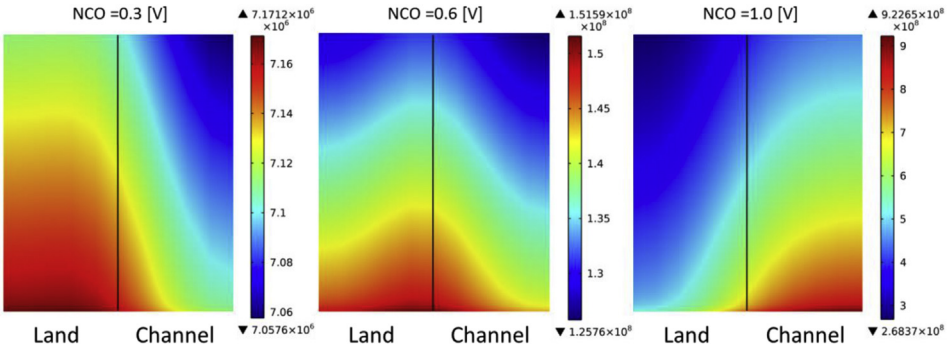

Fig. 9. Volumetric current density along the membrane/CL interface (x–y plane) (A m^{-3}).

dominate and hence the highest reaction rates occur under the channel region. Finally, at intermediate current densities (NCO = 0.6 V), Fig. 9 indicates that the reaction zone straddles the junction between the land and channel owing to roughly equal contributions from ohmic and mass transport losses; in fact, the reaction rate is maximized at the corner of the land. In addition, Fig. 9 also shows the effect of mass transport loss along the channel. In all cases, the reaction rate decreases away from the inlet, and the longitudinal gradient increases with η_{NCO}.

Results presented thus far show that the coupled modified agglomerate approach is successful at providing the expected results for the 3D PEM fuel cell cathode. Fig. 10 presents polarization curves predicted by the classical spherical agglomerate model, the particle model with and without matched ionomer film thickness, and the macro-homogenous model. It is seen that the macro-homogenous model cannot produce realistic predictions in the mass transport limited region due to an absence of microscale structure that could account for the dissolution and diffusion of reactant in the ionomer. On the other hand, the classical agglomerate model is able to capture the sharp drop-off in current density in the mass transport limited region as seen in Fig. 10. It should be noted that the ionomer film is the only diffusion-loss mechanism for the classical agglomerate which neglects the significance of diffusion inside the agglomerate core [33]. On the other hand, the modified particle approach correctly accounts for the significance of diffusion inside the agglomerate core by considering a discrete distribution of particles. Therefore, the particle approach predicts an earlier and sharper drop-off of voltage in the mass transport limited region than the classical approach. However, Fig. 10 shows that when the ionomer film thickness is adjusted in the modified model to match that of the classical model, the overall performances are comparable. Hence, for the comparison purposes, it is appropriate to match the film thickness.

Next we compare the predictions of current density distribution by the three models along a transverse line on the membrane/CL interface close to the outlet. We investigated the ohmic and mass transport loss regions in Figs. 11 and 12, respectively. Fig. 11 indicates that for the ohmic region, all models predict the highest current density close to the corner of the land. It is also seen that the classical and the modified agglomerate model predictions are close to each other throughout. However, while the agglomerate models show a higher current density under the channel, the macro-homogenous model predicts a higher current density under the land. For the mass transport region in Fig. 12, the modified agglomerate model behaves identically with the classical approach. While the agglomerate model predicts the highest current densities under the channel due to mass transport limitations, the macro-homogenous approach continues to predict the highest current density close to the corner. As mentioned earlier, the predictions of the macro-homogenous approach in Figs. 11 and 12 are not realistic because it does not account for the dissolution and diffusion of reactant in the ionomer.

Finally, we investigated the effects of Pt loading on the polarization curve. Figs. 13 and 14 show the effect of Pt loading on polarization curves as predicted by the classical and modified agglomerate models, respectively. Although the trends are similar for both models in the activation and ohmic loss regions, the predictions diverge in the mass transport region. The classical agglomerate model predicts nearly identical limiting currents as in Ref. [19] despite a fourfold increase in Pt loading as seen in Fig. 13.

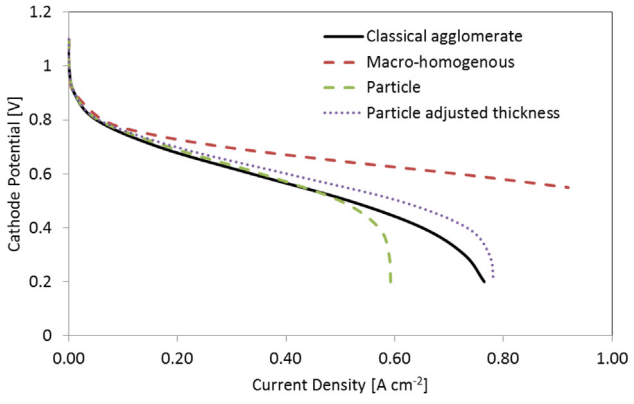

Fig. 10. Comparison of polarization curves for the 3D cathode obtained with different CL modeling approaches.

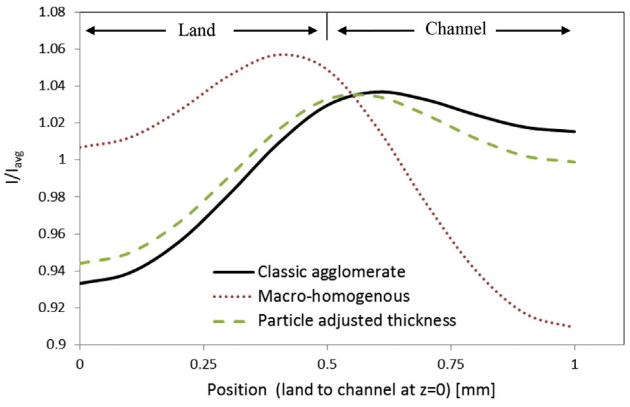

Fig. 11. Comparison of current density distribution from different CL modeling approaches along a line at the membrane/CL interface at $y = 0.98L_{ch}$ and $I_{avg} = 0.4$ A cm^{-2}.

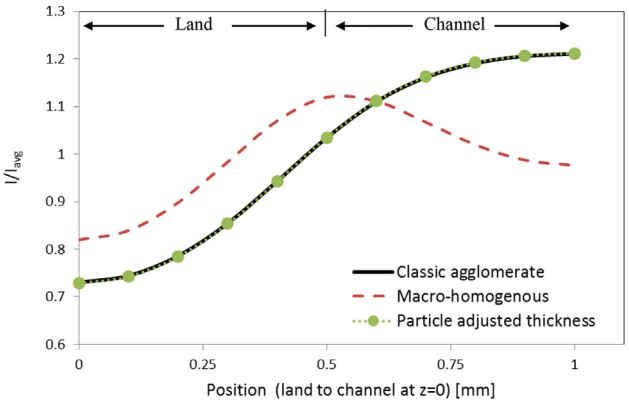

Fig. 12. Comparison of current density distribution from different CL modeling approaches along a line at the membrane/CL interface at $y = 0.98L_{ch}$ and $I_{avg} = 0.77$ A cm^{-2}.

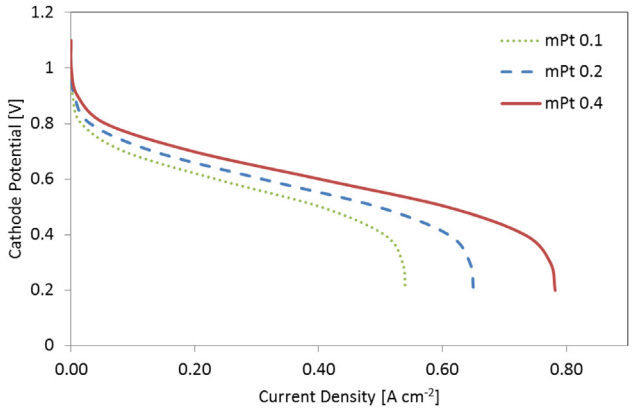

Fig. 14. Polarization curves for various Pt loadings (m_{Pt}) in mg cm^{-2} predicted by the modified agglomerate model.

This is because diffusion losses in the classical agglomerate model are dominated by the ionomer film which imposes the same limiting current irrespective of Pt loading inside the core [33]. On the other hand, experimental results in Ref. [50] show that Pt loading affects the performance and the limiting current. The modified approach correctly accounts for the significance of diffusion inside the agglomerate core by modeling the particle-level effects. Therefore, the particle model is sensitive to Pt loading in the mass transport loss region as shown in Fig. 14.

It should be noted that it is possible obtain different limiting currents even with the classical agglomerate model by setting relations between the agglomerate and CL structural parameters. For instance, Refs. [20–22,26,27] incorporated changes in the CL structure by varying the number of agglomerates per unit volume which concurrently changes the total effective agglomerate surface area (a_{agg}). However, none of these is equivalent to incorporating the effect of particle-level diffusion losses in the microscale model.

4. Summary and conclusions

.In this study, we employed a modified agglomerate approach based on discrete catalyst particles [33] to build a 3D model for the PEM fuel cell cathode. The effect of random agglomerate structure and nanoscale diffusion losses are incorporated within a 3D PEM fuel cell model for the first time. The microscale-to-macroscale coupling procedure employed in the classical agglomerate approach in Ref. [19] was modified to permit the use of numerical results from the modified agglomerate microscale model. The novel 3D cathode model was found to produce expected results for species concentration, overpotential, and reaction rate distributions in the cathode.

By comparing the predictions of the modified model with the classical and macro-homogeneous models, it was shown that the modified approach provided results that matched with the classical approach under all operating regimes. However, the macro-homogenous model, which ignores the importance of microscale effects, fails to successfully predict mass transport losses.

In addition, the modified approach is superior to the classical approach in predicting the effect of Pt loading inside the agglomerate core. The modified model exhibits sensitivity to Pt loading even in the mass transport loss region, whereas the classical approach provides nearly identical results irrespective of Pt loading.

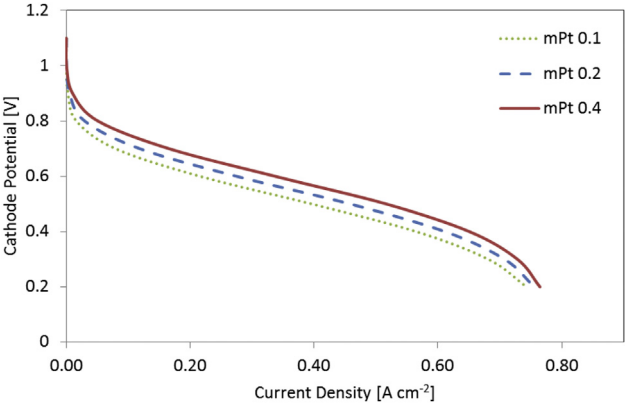

Fig. 13. Polarization curves for various Pt loadings (m_{Pt}) in mg cm^{-2} predicted by the classical agglomerate model.

Acknowledgments

This work was conducted under the University of Delaware's Fuel Cell Bus Program to research, build, and demonstrate fuel cell powered hybrid vehicles for transit applications. This program is funded by the Federal Transit Administration at the Center for Fuel Cell Research at the University of Delaware.

Nomenclature

A_0	surface area per unit weight of Pt [cm^2 g^{-1}]
a_{Pt}	total effective reaction area [m^2 m^{-3}]
a_{agg}	effective agglomerate surface area [m^2 m^{-3}]
C_{O_2}	local oxygen concentration [mol m^{-3}]
C	oxygen concentration in agglomerate core [mol m^{-3}]
C_f	oxygen concentration in ionomer film [mol m^{-3}]
C_s	agglomerate surface oxygen concentration [mol m^{-3}]
C_0	ionomer film surface oxygen concentration [mol m^{-3}]
$C_{O_2,ref}$	reference oxygen concentration [mol m^{-3}]
$D_{i,j}$	binary diffusivities of i and j [m^2 s^{-1}]
$D_{i,j}^{eff}$	effective binary diffusivities of i and j [m^2 s^{-1}]
D	diffusivity of oxygen in ionomer [m^2 s^{-1}]
D_{eff}	effective diffusivity of oxygen in ionomer [m^2 s^{-1}]
E_{th}	Nernst voltage
H	Henry's constant [atm m^3 mol^{-1}]
i	current density [A cm^{-2}]
$\nabla.i$	volumetric current density [A cm^{-3}]
i_0^{ref}	reference exchange current density [A cm^{-2}]
k_c	reaction rate constant [s^{-1}]
M_n	molecular weight of gas mixture [kg mol^{-1}]

M_j	molecular weight of species j [kg mol^{-1}]
m_{Pt}	Pt loading [mg cm^{-2}]
N_{O_2}	oxygen flux [mol m^{-2} s^{-1}]
P	pressure [atm]
P_{O_2}	oxygen partial pressure [atm]
P_{H_2}	hydrogen partial pressure [atm]
Pt|C	platinum carbon weight ratio
R_{O_2}	volumetric oxygen reaction rate [mol m^{-3} s^{-1}]
R_{HO_2}	volumetric reaction rate for water vapor [mol m^{-3} s^{-1}]
r_{agg}	agglomerate radius [m]
r_{Pt}	Pt particle radius [m]
T	temperature [K]
Th	Thiele modulus
t_{cl}	catalyst layer thickness [m]
α_c	charge transfer coefficient
α_{OD}	osmotic drag coefficient
δ	ionomer film thickness [m]
ε_{GDL}	porosity of GDL
ε_{CL}	porosity of CL
ε_{agg}	ionomer volume fraction in agglomerate
η_{NCO}	nominal cathode overpotential
λ	local water content
μ	dynamic viscosity [kg m^{-1} s^{-1}]
ρ	density [kg m^{-3}]
σ_s	electron conductivity [S m^{-1}]
σ_s^{eff}	effective electron conductivity [S m^{-1}]
σ_m	ionic conductivity [S m^{-1}]
σ_m^{eff}	effective ionic conductivity [S m^{-1}]
φ	local overpotential [V]
ϕ_s	electron potential [V]
ϕ_m	ionic potential [V]
ϕ_{RH}	local relative humidity
ψ	Thiele modulus
ω_i	mass fraction of species i

References

[1] T. Berning, D.M. Lu, N. Djilali, J. Power Sources 106 (1–2) (2002) 284–294.
[2] D. Harvey, J.G. Pharoah, K. Karan, J. Power Sources 179 (2008) 209–219.
[3] Y.W. Rho, S. Srinivasan, Y.T. Kho, J. Electrochem. Soc. 141 (8) (1994) 2089–2096.
[4] Q. Wang, M. Eikerling, D. Song, Z. Liu, T. Navessin, Z. Xie, S. Holdcroft, J. Electrochem. Soc. 151 (7) (2004) A950–A957.
[5] M. Eikerling, A.A. Kornyshev, J. Electroanal. Chem. 453 (1–2) (1998) 89–106.
[6] D.M. Bernardi, M.W. Verbrugge, AIChE J. 37 (8) (1991) 1151–1163.
[7] C. Marr, X. Li, J. Power Sources 77 (1) (1999) 17–27.
[8] D. Song, Q. Wang, Z. Liu, T. Navessin, M. Eikerling, S. Holdcroft, J. Power Sources 126 (12) (2004) 104.
[9] T.E. Springer, M.S. Wilson, S. Gottesfeld, J. Electrochem. Soc. 140 (12) (1993) 3513–3526.
[10] K. Broka, P. Ekdunge, J. Appl. Electrochem. 27 (3) (1997) 281–289.
[11] S.H. Chan, W.A. Tun, Chem. Eng. Technol. 24 (1) (2001) 51–57.
[12] N.P. Siegel, M.W. Ellis, D.J. Nelson, M.R. von Spakovsky, J. Power Sources 115 (2003) 81–89.
[13] F. Jaouen, G. Lindbergh, G. Sundholmb, J. Electrochem. Soc. 149 (4) (2002) A437–A447.
[14] Baschuk, Li, J. Power Sources 86 (2000) 181–196.
[15] D.H. Schwarz, N. Djilali, J. Electrochem. Soc. 154 (11) (2007) B1167–B1178.
[16] Q. Wang, M. Eikerling, D. Song, Z. Liu, J. Electroanal. Chem. 573 (2004) 61–69.
[17] M. Yin, J. Electrochem. Soc. 152 (3) (2005) A583–A593.
[18] R.M. Rao, R. Rengaswamy, J. Power Sources 158 (2006) 110–123.
[19] W. Sun, B.A. Peppley, K. Karana, Electrochim. Acta 50 (2005) 3359–3374.
[20] S. Kamarajugadda, S. Mazumder, J. Power Sources 183 (2008) 629–642.
[21] M. Srinivasarao, D. Bhattacharyya, R. Rengaswamy, S. Narasimhan, Chem. Eng. Res. Des. 89 (2011) 10–22.
[22] S. Obut, E. Alper, J. Power Sources 196 (2011) 1920–1931.
[23] Y. Tabe, M. Nishino, H. Takamatsu, T. Chikahisa, J. Electrochem. Soc. 158 (10) (2011) B1246–B1254.
[24] P. Jain, L.T. Biegler, M.S. Jhon, Electrochemical and Solid-State Letters 11 (10) (2008) B193–B196.
[25] W. Yoon, A.Z. Weber, J. Electrochem. Soc. 158 (8) (2011) B1007–B1018.
[26] M. Secanell, K. Karan, A. Suleman, N. Djilali, Electrochim. Acta 52 (2007) 6318–6337.
[27] M. Secanell, Ph.D. Dissertation, University of Victoria, 2007.
[28] R.M. Rao, R. Rengaswamy, Chem. Eng. Res. Des. 84 (A10) (2006) 952–964.
[29] R.M. Rao, D. Bhattacharyya, R. Rengaswamy, S.R. Choudhury, J. Power Sources 173 (2007) 375–393.
[30] P. Jain, L.T. Biegler, M.S. Jhon, J. Electrochem. Soc. 157 (8) (2010) B1222–B1229.
[31] W.K. Epting, S. Lister, Int. J. Hydrogen Energy 37 (2012) 8505.
[32] S. Kamarajugadda, S. Mazumder, J. Power Sources 208 (2012) 328–339.
[33] F.C. Cetinbas, S.G. Advani, A.K. Prasad, J. Electrochem. Soc. 160 (8) (2013) F750–F756.
[34] G. Wang, P.P. Mukherjee, C.-Y. Wang, Electrochim. Acta 51 (2006) 3139–3150.
[35] G. Wang, P.P. Mukherjee, C.-Y. Wang, Electrochim. Acta 51 (2006) 3151–3160.
[36] G. Wang, P.P. Mukherjee, C.-Y. Wang, Electrochim. Acta 52 (2007) 6367–6377.
[37] T. Hattori, A. Suzuki, R. Sahnoun, M. Koyama, H. Tsuboi, N. Hatakeyama, A. Endou, H. Takaba, M. Kubo, C.A.D. Carpio, et al., Appl. Surf. Sci. 254 (2008).
[38] S.H. Kim, H. Pitsch, J. Electrochem. Soc. 156 (2009) 673–681.
[39] N.A. Siddique, F. Liu, Electrochim. Acta 55 (2010) 5357–5366.
[40] K.J. Lange, P.-C. Sui, N. Djilali, J. Electrochem. Soc. 157 (2010) 1434–1442.
[41] K.J. Lange, P.-C. Sui, N. Djilali, J. Power Sources 196 (2011) 3195–3203.
[42] J. Zhang, W. Yang, L. Xu, Y. Wang, Electrochim. Acta 56 (2011) 6912–6918.
[43] K.J. Lange, P.-C. Sui, N. Djilali, J. Power Sources 208 (2012) 354–365.
[44] E.L. Cussler, Diffusion-mass Transfer in Fluid Systems, second ed., Cambridge University Press, Cambridge, 1997.
[45] T.E. Springer, T.A. Zawodzinski, S. Gottesfeld, J. Electrochem. Soc. 138 (8) (1991).
[46] A. Parthasarathy, C.R. Martin, S. Srinivasan, J. Electrochem. Soc. 138 (4) (1991) 916.
[47] A. Parthasarathy, S. Srinivasan, A.J. Appleby, C.R. Martin, J. Electrochem. Soc. 139 (9) (1992) 2530.
[48] A. Parthasarathy, S. Srinivasan, A.J. Appleby, C.R. Martin, J. Electrochem. Soc. 139 (10) (1992) 2856.
[49] H.S. Fogler, Elements of Chemical Reaction Engineering, third ed., Prentice Hall PTR, 2000.
[50] Z. Qi, A. Kaufman, J. Power Sources 113 (2003) 37.